



Original

Napolitano, D.; da Silveira, I.; Tandon, A.; Calil, P.:

Submesoscale Phenomena Due to the Brazil Current Crossing of the Vitória-Trindade Ridge.

In: Journal of Geophysical Research : Oceans. Vol. 126 (2021) 1, e2020JC016731.

First published online by AGU: 06.12.2020

<https://dx.doi.org/10.1029/2020JC016731>

Submesoscale Phenomena Due to the Brazil Current Crossing of the Vitória-Trindade Ridge

 D. C. Napolitano^{1,2} , I. C. A. da Silveira¹ , A. Tandon³ , and P. H. R. Calil⁴ 

¹Instituto Oceanográfico, Universidade de São Paulo, São Paulo, Brazil, ²Now at Laboratoire d'Études en Géophysique et Océanographie Spatiales (LEGOS), CNES-OMP-IRD-CNRS-UPS, Toulouse, France, ³Department of Mechanical Engineering, University of Massachusetts Dartmouth, North Dartmouth, MA, USA, ⁴Institute of Coastal Research, Helmholtz-Zentrum Geesthacht, Geesthacht, Germany

Key Points:

- Observations capture submesoscale structures associated with western boundary currents due to the crossing of a seamount chain
- Observed and modeled unstable flow occur below the mixed layer and are prone to partially resolved symmetric instabilities
- Flow-topography interactions mask seasonality in the region's submesoscale activity

Correspondence to:

D. C. Napolitano,
dante.napolitano@legos.obs-mip.fr

Citation:

Napolitano, D. C., da Silveira, I. C. A., Tandon, A., & Calil, P. H. R. (2020). Submesoscale phenomena due to the Brazil Current crossing of the Vitória-Trindade Ridge. *Journal of Geophysical Research: Oceans*, 125, e2020JC016731. <https://doi.org/10.1029/2020JC016731>

Received 20 AUG 2020

Accepted 1 DEC 2020

Abstract At 20.5°S, the Brazil Current and the Intermediate Western Boundary Current interact with a quasi-zonal seamount chain, the Vitória-Trindade Ridge (VTR). While the mesoscale variability generated due to these western boundary currents crossing the VTR has been recently studied, the submesoscale dynamics associated with such features have never been addressed. Here, we use new observations and a 2-km-resolution model to analyze the role of the VTR seamounts in the regional submesoscale dynamics, their seasonality, and instabilities. We present new high-resolution velocity and density observations that capture submesoscale features associated with the flow. Within these regions, potential vorticity (PV) reveals patches of symmetrically unstable flow close to seamounts. The horizontal resolution ($\Delta x \approx 1.5$ km) of our quasi-synoptic observations (10 h) partially resolves submesoscale instabilities. Our Regional Oceanic Modeling System simulation identifies two regimes of submesoscale activity in the region, one typically associated with the seasonal cycle of the mixed layer, and a second associated with flow-topography interactions. A spatiotemporal analysis of the vertical buoyancy fluxes points to these flow-topography interactions as the main source of recurrent, deeper instabilities. As the VTR emerges as a submesoscale hotspot in the oligotrophic South Atlantic, the lack of observations still remains the main obstacle to better understand submesoscale processes in the region.

Plain Language Summary At 20.5°S, strong currents interact with a submarine chain, the Vitória-Trindade Ridge (VTR). In this study, we use new observations and a 2-km-resolution regional numerical model to analyze how the interaction between the Brazil Current (BC) and the VTR seamounts give rise to submesoscale instabilities. We present new high-resolution velocity and density observations that capture submesoscale features associated with the flow, with patches of unstable flow associated with the BC interacting with the seamounts. In the same transects of the cruise, our simulation shows that submesoscale activity follows a typical seasonal cycle. But this seasonality is masked in regions where the flow intercepts topography. A spatiotemporal analysis of the vertical fluxes points to flow-topography interactions as the main source for these recurrent, deeper instabilities. As the VTR emerges as a submesoscale hotspot in the oligotrophic South Atlantic, the lack of observations still remains the main obstacle to better understand the submesoscale processes in the region.

1. Introduction

At latitudes north of which it becomes a robust western boundary current, the newly formed, poleward-flowing Brazil Current (BC) encounters a zonal seamount chain—the Vitória-Trindade Ridge (VTR). Located at 20.5°S, with seamounts reaching up to 30 m below the surface, the VTR poses an obstacle for the typically 150-m-deep BC southward path (Costa et al., 2017; Evans et al., 1983). Underneath the BC, the Intermediate Western Boundary Current (IWBC) flows equatorward, crossing the ridge in the opposite direction (Legeais et al., 2013; Napolitano et al., 2019). From 28°S to 21°S, the two opposing flows of the BC and the IWBC compose the so-called BC System (Silveira et al., 2004). The currents are generally vertically aligned, and frequently interact (e.g., Mano et al., 2009; Silveira et al., 2004; Silveira et al., 2008). Downstream of the VTR, at 21.6°S, where the BC reattaches to the slope after crossing the ridge, new microstructure data suggested that vertical shear below the surface mixed layer may drive intense turbulent mixing activity (Lazaneo et al., 2020). Individually, the BC and the IWBC cross the VTR in opposite directions, negotiating its channels and seamounts. The IWBC develops topographically forced structures and strong mesoscale activity

(e.g., Costa et al., 2017; Legeais et al., 2013; Napolitano et al., 2019). The BC also develops mesoscale eddies up and downstream the ridge, for example, the cyclonic Vitória Eddy (Arruda & Silveira, 2019; Schmid et al., 1995) and the anticyclonic Abrolhos Eddy (Soutelino et al., 2011, 2013).

Submesoscale motions in the ocean are characterized by horizontal scales of $\mathcal{O}(1\text{--}10)$ km, vertical scales of $\mathcal{O}(10)$ m, and timescales of $\mathcal{O}(1)$ day (Capet et al., 2007). At these scales, typical mesoscale Rossby [$U / fL \ll \mathcal{O}(1)$] and Richardson [$N^2 H^2 / U^2 \gg \mathcal{O}(1)$] numbers become $\mathcal{O}(1)$ in localized regions (Mahadevan & Tandon, 2006). There, the dynamics are governed by submesoscale, which bridges hydrostatic to nonhydrostatic motions, and leads to vertical velocities of $\sim 100 \text{ mday}^{-1}$ [$\mathcal{O}(10^{-3}) \text{ ms}^{-1}$] within the mixed layer, against the observed $\sim 1 \text{ mday}^{-1}$ [$\mathcal{O}(10^{-5}) \text{ ms}^{-1}$] of the mesoscale (Thomas et al., 2008).

Earlier studies have hinted at the importance of ocean fronts by showing that they are preferential regions for the generation of large vertical velocities and the emergence of ageostrophic dynamics (e.g., Pollard & Regier, 1992; Rudnick, 1996). Klein et al. (1998) investigated the stirring of thermohaline anomalies and identified sharp thermohaline fronts driven by the mesoscale eddy field. At these fronts, the three-dimensional ageostrophic circulation is key in controlling their dynamics, strength, and spatial distribution. Mahadevan and Archer (2000) modeled the impact of fronts on the mesoscale nutrient supply at different spatial resolutions. Their study identified that processes occurring at the scale of the fronts were not properly resolved by mesoscale. More recent investigations have accounted for submesoscale dynamics responsible for these and other important processes, such as mixed-layer restratification (e.g., Boccaletti et al., 2007), regulation of primary productivity (e.g., Lévy et al., 2012), the vertical motion and distribution of tracers in the upper ocean (e.g., Calil, 2017; Mahadevan & Tandon, 2006; Thomas et al., 2008), and the forward cascade of energy (e.g., Capet et al., 2008).

New technologies and techniques allowed in situ observations of submesoscale processes. Rocha, Chereskin, et al. (2016) analyzed 13 years of shipboard-ADCP data across Drake Passage, showing that ageostrophic motions account for half of the surface kinetic energy at scales of $\mathcal{O}(10)$ km. Also in the Drake Passage, Viglione et al. (2018) used gliders to show that submesoscale motions evolved differently in distinct geographical locations. Ramachandran et al. (2018) observed dynamical signatures indicative of submesoscale processes at a salinity front in the Bay of Bengal. Latest developments in submesoscale sampling include the observation of two-dimensional velocity gradients (e.g., saildrone fleets; Voosen, 2018).

Studies concerning flow-topography interactions at submesoscale (e.g., Naveira Garabato et al., 2019; Ruan et al., 2017) are recent and less common in the literature. It is known that islands and seamounts occupy less than 5% of the ocean floor (Rogers, 2019). They interact with the adjacent flow boosting ocean processes, such as diapycnal mixing (e.g., Lueck & Mudge, 1997), generation and breaking of internal waves (e.g., Nikurashin & Ferrari, 2010), and dissipation of kinetic energy (e.g., Naveira Garabato et al., 2004). These flow-topography interactions may inject enough shear into the mesoscale field, leading to the formation of smaller scale eddies and filaments (cf. Benthuyssen & Thomas, 2012; D'Asaro, 1988; Gula et al., 2016; McWilliams, 2016; Molemaker et al., 2015; Morvan et al., 2019). Although the precise BC path through the VTR is still uncertain, the current must cross this seamount-populated area, where submesoscale-resolution observations are scarce.

In this study, we provide new observations—with enough horizontal resolution to capture the submesoscale variability associated with the BC and the IWBC crossing the VTR—and a submesoscale-permitting numerical simulation. We aim to (1) describe the observed submesoscale-like features and test their instability criteria, (2) characterize the submesoscale instabilities and their seasonality, and (3) analyze the role of the VTR seamounts in the BC submesoscale dynamics.

2. Submesoscale Observations

2.1. The *Ilhas Austral* Summer Expedition

In order to study flow-topography interactions in the VTR, we use velocity data from a 75-kHz shipboard Acoustic Doppler Current Profiler (sADCP), density derived from a towed Underway Conductivity, Temperature and Depth probe (uCTD), and local topography data from 12 and 38 kHz vessel-mounted Echosounder.

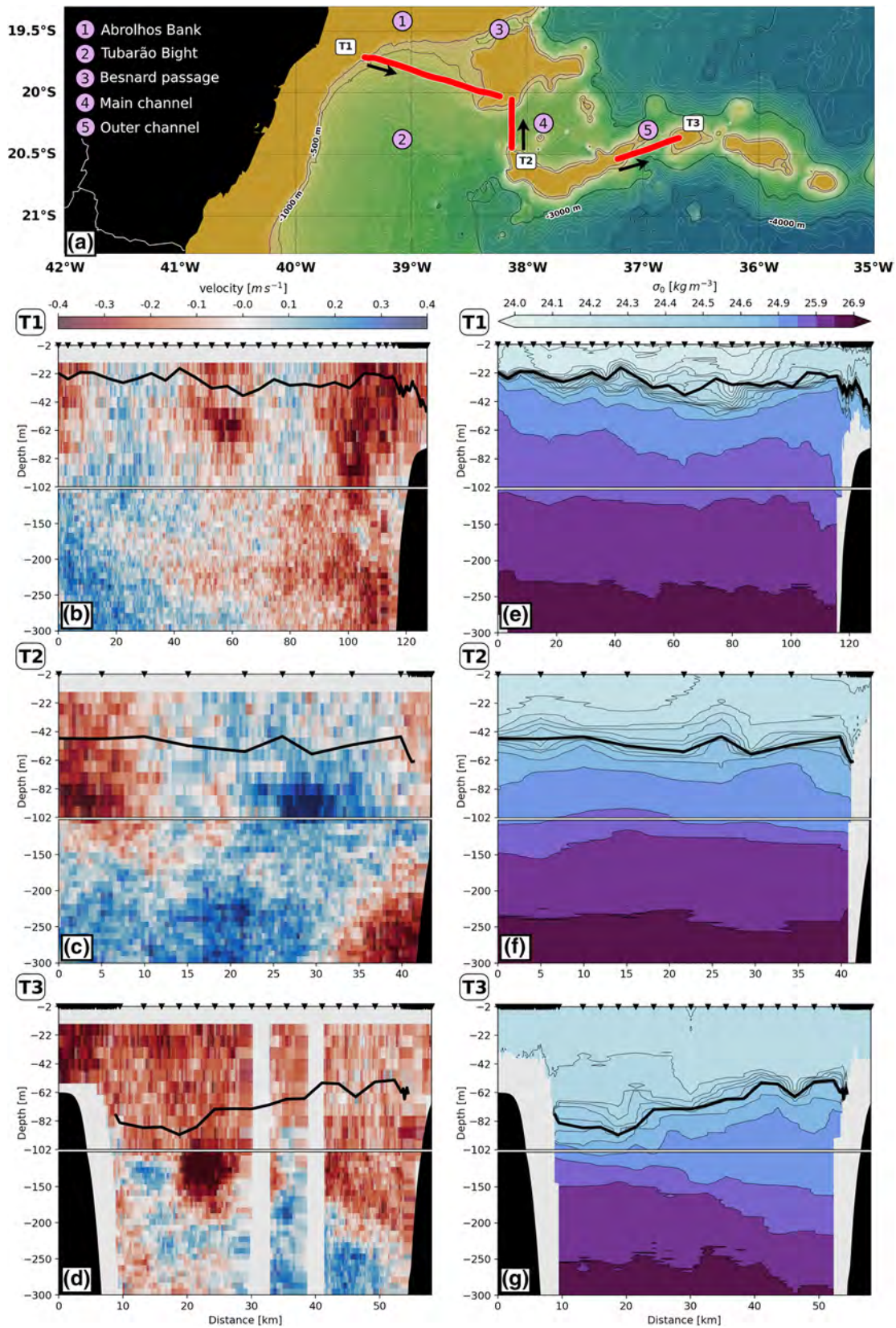
We obtained the data from a 20-day cruise that took place in the austral summer of 2017 (from January 27 to February 16) onboard the RV Alpha Crucis. We analyzed data from the three westernmost transects of the entire data set, that is, in the region where the BC flows through the seamounts of the VTR (see Figure 1a). Our sampling strategy—with transects perpendicular to the main channels and timescales smaller than internal-tide periods—aimed to reduce the effect of internal and topographic lee waves, known to be important in the region (Morozov, 1995; Paiva et al., 2018; Zhao et al., 2016). At each transect, the velocity and mass structure data are synoptic: in transects T1–T3, we covered approximately 125, 45, and 60 km in about 11, 7, and 7 h, respectively. The longer transect (T1) occupied less than $1/3$ of the inertial period ($2\pi/f$), estimated to be ~ 35 h in the region. Since transects were sampled faster than the inertial timescales of the submesoscale, we may estimate the spatial gradients at each transect from the synoptic snapshots (Thomas et al., 2008).

Figure 1 displays the synoptic picture obtained for the three transects during the *Ilhas* survey. We processed the short-time averaged (120 s) sADCP data using the CODAS package (Firing et al., 1995). We then manually removed spurious data, which bypassed the previous processing stages, and discard the data acquired during stations. Using only downcast temperature and salinity profiles from the uCTD casts, we calculated the σ_0 potential density. To define the mixed-layer depth (MLD), we modified the difference criteria (e.g., Montégut et al., 2004), and set it as the depth of 0.25 kgm^{-3} increment from the value of σ_0 at 2 m. South of Abrolhos Bank, transect T1 (Figures 1b and 1e) exhibits a 0.5 ms^{-1} jet flowing past the topography, probably escaping through the Besnard Passage into the Tubarão Bight. Altimeter-derived velocities (not shown) indicate this ~ 30 km-wide jet to be a branch of the BC. Our data show the BC as a 100 m-deep jet, which is not constrained by the summer shallow MLD of ~ 30 m, and occupies the upper seasonal pycnocline. At 90 km from the beginning of the transect, outcropping isopycnals mark the limit of the jet, forming a sharp front (Figure 1e). Between ~ 50 and 60 km, at 40–60 m depth, we depict a 10 km-wide patch of higher velocities, which suggests the presence of a shingle (Stern, 1985) shed by the BC. On the density section, small lenses within the pycnocline, between 40 and 80 km, hint at the presence of submesoscale anticyclonic intrathermocline eddies (cf. D'Asaro, 1988; McWilliams, 1985). Below 150 m in Figure 1b, T1 captures the quasipermanent, 0.2 ms^{-1} IWBC cyclonic recirculation, as described by Costa et al. (2017) and Napolitano et al. (2019). Also, some of the observed features in T1 (and subsequent observations) may result from internal lee waves that are generated by the flow impinging on small-scale topography, with frequency and scales set by the currents' strength and the seamount topography (Whalen et al., 2020).

The south–north-oriented transect T2 (Figures 1c and 1f) cuts through the Main channel of the VTR. A second 100-m-deep, 10-km wide branch of the BC flows westward close to the northern bank at 0.5 ms^{-1} . Below the 50-m mixed layer, a 10-km wide counterflow is also seen at 30 km, indicating either a recirculation of the BC, a cyclonic eddy, or a detached filament (Figure 1c). Density from T2 displays two distinct interthermocline eddies within the MLD, centered at 5 and 25 km; at 80 m, a slightly displaced isopycnal suggests the presence of a cyclone, with the smaller eddies at its border (Figure 1f). The IWBC at about 0.5 ms^{-1} strength escaping Tubarão Bight through the main channel is captured on the northern 30 km of T2; at the southern end of T2, below 200 m, a patch of opposite (westward) velocities is seen next to the seamount (Figure 1c), possibly associated with lateral shear between the IWBC and the seamount topography, or with a recirculation within the main channel.

At 37°W , a band of southward velocities spans across the outer channel in transect T3 (Figures 1d and 1g). The highest surface velocities occur on top of the westbound seamount. The maximum MLD is 90 m, shoaling 40 m from west to east, where isopycnals are packed and stratification is strong. Below 200 m, a northward-flowing branch of the IWBC crosses the ridge through this channel, which agrees with the modeling results of Costa et al. (2017).

On the western portion of T3, a strong southward flow ($>0.7 \text{ ms}^{-1}$) appears in a background of northward flow. This pattern is consistent with an intrathermocline dipole of southward propagation, where the central southward flow represents the interface between the two eddies. Either a dipole, a filament, or an isolated intrathermocline eddy, this structure—as well as the counterflow observed in T2—is likely to develop due to lateral shear between the IWBC and the seamount topography. This mechanism of eddy generation due to flow-topography interactions due to lateral friction was first proposed by D'Asaro (1988), during



the observation of submesoscale eddies in the Arctic Ocean. More recent studies also account for bottom boundary layer friction inducing eddy formation (e.g., Benthuisen & Thomas, 2012; Morvan et al., 2019).

2.2. Observational Evidence of Submesoscale Instabilities at the Vitória-Trindade Ridge

Submesoscale instabilities act on the forward cascade of kinetic energy, conveying energy from the mesoscale *en route* to dissipation (Capet et al., 2008). In the process, ageostrophic secondary circulations arise from different types of baroclinic submesoscale instabilities, leading to restratification. Gravitational instability occurs when there is gain of kinetic energy via buoyancy fluxes in the presence of unstable stratification ($N^2 < 0$), which consumes readily available potential energy (Thomas et al., 2013). Frontal instabilities present a secondary circulation associated with frontal shear (Molemaker et al., 2010). This class of instability includes symmetric instability—which extracts kinetic energy from the vertical shear of geostrophic flows (cf. Taylor & Ferrari, 2010; Thomas et al., 2013)—and ageostrophic baroclinic instability, which extracts available potential energy by slumping isopycnals (cf. Fox-Kemper et al., 2008). While symmetric instabilities are essentially two-dimensional, ageostrophic baroclinic instabilities also result in vertical fluxes. Inertial instability (a.k.a. centrifugal instability) develops in anticyclonic motions with relative vorticity ($\zeta \equiv v_x - u_y$) stronger than planetary vorticity (f), drawing energy from the horizontal shear of the flow (cf. Gula et al., 2016; Thomas et al., 2013). According to Thomas et al. (2013), these instability types can be differentiated by their sources of kinetic energy. This can be conveniently visualized by the angle

$$\phi_{RiB} = \tan^{-1}(-Ri_B^{-1}). \quad (1)$$

Where the balanced Richardson number is defined as

$$Ri_B = \frac{N^2 f^2}{M^4}. \quad (2)$$

Both N^2 and M^4 relate to the spatial variations of the buoyancy, defined as $b \equiv -g(\rho/\rho_0)$, where g is the acceleration due to gravity, ρ is the density, and $\rho_0 = 1,025 \text{ kg m}^{-3}$ is the reference density. $N^2 \equiv b_z$ is the stratification, and $M^4 \equiv b_x^2 + b_y^2$ is the magnitude of the lateral buoyancy gradient (subscripts indicate derivatives in the corresponding Cartesian directions).

Thomas et al. (2013) state that the instability is gravitational when $-180^\circ < \phi_{RiB} < -135^\circ$ and is a hybrid of gravitational and symmetric when $-135^\circ < \phi_{RiB} < -90^\circ$. For anticyclonic ζ , symmetric instability arises for $-90^\circ < \phi_{RiB} < -45^\circ$ and a hybrid of symmetric and inertial instability occur for $-45^\circ < \phi_{RiB} < \phi_c$ (ϕ_c is a critical, geostrophic Rossby number). Cyclonic ζ yields symmetric instability for $-90^\circ < \phi_{RiB} < \phi_c$. To properly employ such classification, however, observations and numerical modeling should fully resolve these instabilities, demanding small-scale measurements (e.g., D'Asaro et al., 2011; Nagai et al., 2012) and large eddy simulations with a grid resolution of $\mathcal{O}(1)$ aspect ratio (e.g., Stamper & Taylor, 2017; Thomas et al., 2013).

Observations during the Ilhas summer cruise typically have a horizontal resolution Δx spanning ≈ 200 m to 4.5 km, and vertical resolution $\Delta z = 8$ m for the sADCP. For the uCTD, these resolutions are $\Delta x \approx 90$ m to 6.5 km and $\Delta z = 1$ m. (Higher resolution at the seamount-slopes reduced the mean Δx and yielded greater deviations in the uCTD measurements.) We perform an objective analysis (correlation lengths $x = 5$ km and $z = 25$ m) based on the sADCP vertical resolution and the uCTD horizontal resolution (i.e., the coarser resolution comparing both instruments). To better understand the limitations imposed by the scales of the Ilhas data set, we calculate the length and timescales for symmetric instability, for example, Bachman et al. (2017),

Figure 1. The Ilhas austral summer survey. (a) Vitória-Trindade Ridge region map with the dark yellow shading representing depths shallower than 300 m. Red lines indicate the location of transects T1, T2, and T3. (b–d) Short-time averaged shipboard-ADCP cross-transect velocities with a blowout on the upper 100 m. Red pixels represent southward/westward velocities, while blue pixels represent northward/eastward velocities. (e–g) Underway-CTD density with a blowout on the upper 100 m. Darker colors represent denser waters. The black thick line shows the depth of the mixed layer. Black triangles mark the position of the uCTD casts. ADCP, Acoustic Doppler Current Profiler; CTD, Conductivity, Temperature and Depth probe.

$$L_{sym} = 2 \frac{U}{|f|} \sqrt{1 - Ri_B}, \text{ and } T_{sym} = \frac{H}{U} \frac{\sqrt{Ri_B}}{\sqrt{1 - Ri_B}}, \quad (3)$$

and for ageostrophic baroclinic instability according to Fox-Kemper et al. (2008),

$$L_{abi} = 2\pi \frac{U}{|f|} \sqrt{\frac{2}{5}(1 + Ri_B)}, \text{ and } T_{abi} = \sqrt{\frac{54}{5}} \frac{\sqrt{(1 + Ri_b)}}{|f|}. \quad (4)$$

We replace the parameters in Equations 3 and 4 with typical scales for the BC in the VTR region, $0.01 \leq U \leq 0.5 \text{ ms}^{-1}$, $30 \leq H \leq 130 \text{ m}$. In Ri_B conditions favorable for symmetric instability ($0.25 \leq Ri_B \leq 0.95$, see Stone, 1966), $L_{sym} = 100 \text{ m} - 15 \text{ km}$, $T_{sym} = 1 \text{ min} - 15 \text{ h}$, $L_{abi} = 1 - 55 \text{ km}$, and $T_{abi} = 20 - 25 \text{ h}$. Therefore, our data set of quasisynoptic observations (10 h) and gridded at $\Delta x \simeq 1.5 \text{ km}$ only partially resolves modes of symmetric and ageostrophic baroclinic instabilities. The reader should be aware that, whenever we classify “symmetric instabilities” hereafter, it is implicit that we are only dealing with the partial modes discussed above, that is, the larger scale part of the submesoscale.

We assess our observations for unstable flow conditions by calculating the two-dimensional Ertel PV q_{2D} using the same one-ship approximation employed in recent studies, for example, Ramachandran et al. (2018), Viglione et al. (2018), and Lazaneo et al. (2020). We found this approximation justified for the region, testing the q_{2D} against the full-gradient PV calculated from the model outputs. With this assumption, we neglect the across-transect gradients of the PV, expressed as

$$q = (\bar{f}\mathbf{k} + \nabla \times \mathbf{u}) \cdot \nabla b. \quad (5)$$

In Equation 5, $\mathbf{u} = (u, v, w)$ and $\nabla = (\partial_x, \partial_y, \partial_z)$ are the velocity and gradient vectors in Cartesian coordinates, respectively. In the q_{2D} formulation, ζ and M^4 approximate to the along-transect derivative of the cross-transect velocity v and the buoyancy. Therefore,

$$\zeta \approx v_x \quad \text{and} \quad M^2 \approx b_x \quad (6)$$

yield

$$q_{2D} = (\zeta + f)N^2 - v_z M^2. \quad (7)$$

To minimize errors in this approximation, we sailed perpendicular to the VTR channels, where the BC and the IWBC flow through (see Figure 1a, where T1–T3 are perpendicular to the Besnard Passage, the main channel, and the outer channel, respectively). This sampling strategy aimed to reduce the cross-transect gradients ∂_y , compared with the along-transect gradients ∂_x . Nevertheless, the reader must be aware of the limitations of this approximation: ∂_y may be important in some parts of the transect, occasionally compensating or increasing the effects of ∂_x . A thorough analysis of these caveats is presented in Shcherbina et al. (2013).

We made our analysis hemisphere-independent by normalizing the PV. Multiplying Equation 7 by $f/(\beta^2 N^2)$, unstable (or marginally stable) flow regions appear as low and negative PV. Figures 2a–2c show the instantaneous PV for the three transects of the cruise. For every transect, negative PV appears within the upper portion of the mixed layer, close to 20 m. Low PV patches also appear in all transects below 200 m, in regions of weak stratification. Aided by the increased horizontal resolution of the observations near the seamounts, we also find negative PV patches associated with flow close to topography. These regions are detailed in a blowout displayed in Figures 2d–2f.

Figure 2d zooms in on transect T1. Between about 40 and 100 m, an elongated patch of negative PV occurs where the lower portion of the BC rubs against the seamount (see Figure 1b). The negative PV patch in transect T2 (Figure 2e) is the deepest observed in the cruise, next to the seamount between about 150 and 250 m. The region is coincident with a reentrant flow of the IWBC into Tubarão Bight (see Figure 1c). Transect 3 in Figure 2f shows two negative PV patches in the channel comprising two seamounts, associated with

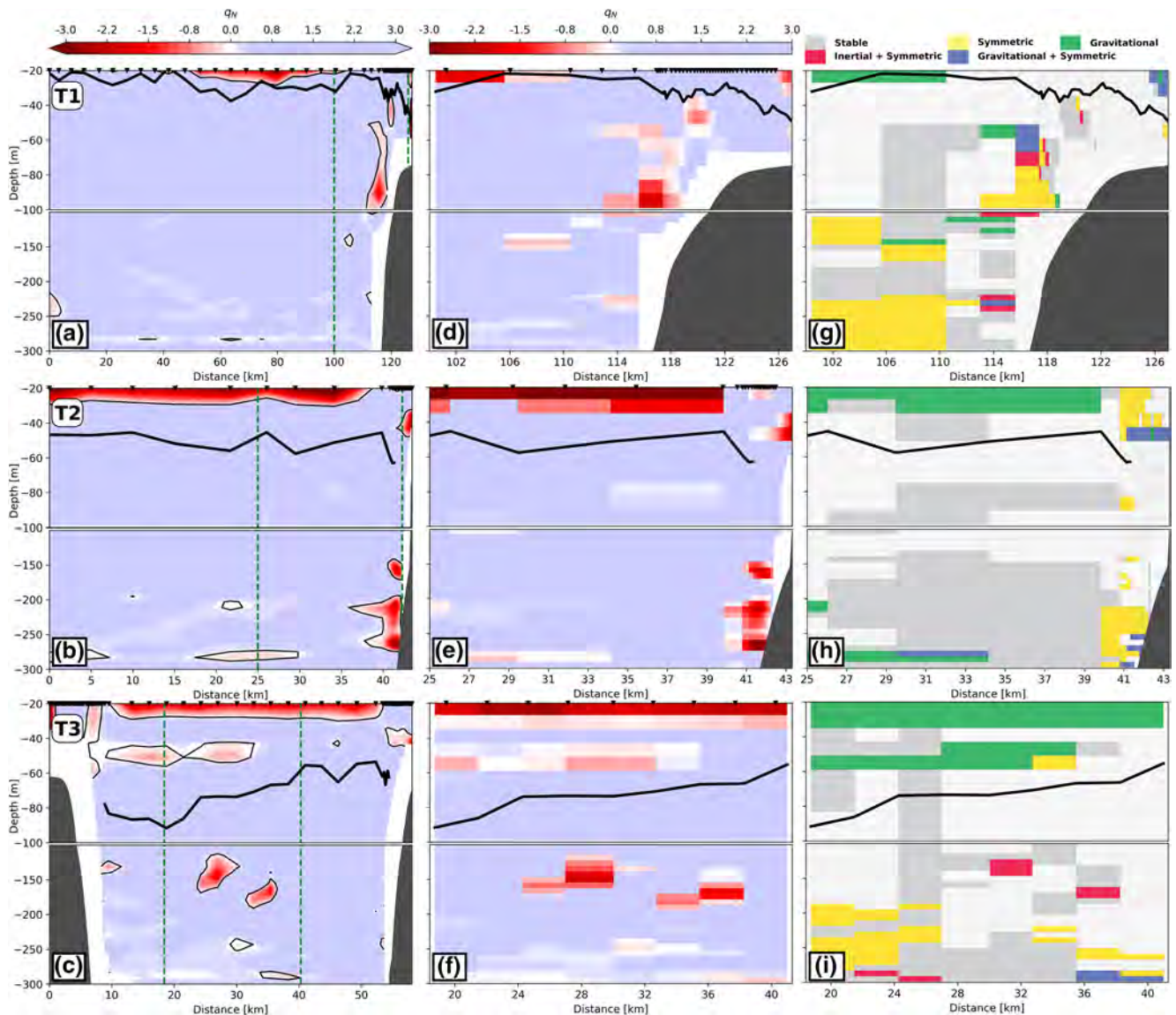


Figure 2. (a–c) Potential vorticity under the 2D approximation for transects T1–T3. Stable q_{2D} regions are shaded in blue, while low and negative PV range from light blue to red. Green dashed lines delimit the blowout region shown in (d–f). (g–i) Instability types for the low PV regions in (d–f), following Thomas’s (2013) classification. The instability types are colored as green for gravitational, blue for gravitational plus symmetric, yellow for symmetric, red for symmetric plus inertial, and gray for stable low PV. PV, potential vorticity.

the anticyclonic portion of the structure observed between 20 and 30 km in Figure 1d. We classify the low PV patches based on the ϕ_{RiB} in Equation 1, following Thomas et al. (2013), for the same blowout regions displayed in Figures 2d–2f. We show our results based on the diagram proposed by these authors, hereafter the “Thomas’s diagram” (see Figure 1 of Thomas et al., 2013). This classification was previously employed by Thompson et al. (2016) and Viglione et al. (2018) for glider observations, with a horizontal resolution similar to ours.

Figures 2g–2i show the instability types observed in the VTR. In all three transects, we observe gravitationally unstable conditions widespread across the upper mixed layer. Such instability is associated with air–sea interactions, which are not extensively discussed in this work (for more information on submesoscale air–sea interactions, see, e.g., [Calil, 2017; Ramachandran et al., 2018; Wenegrat et al., 2018]). Figure 2g shows that, in T1, between 114 and 119 km from its start, symmetric instability and its hybrid forms dominate the unstable regions where the BC flows adjacent to topography. Conditions for symmetric instability also

appear in the low PV region below 200 m, east of 110 km. Figure 2h displays symmetric instability patches close to the topography in T2, where the IWBC reenters Tubarão Bight, between 40 and 43 km. Unstable conditions favoring symmetric instability also appear within the mixed layer. In T3, Figure 2i reveals the inertial-symmetric hybrid instability at 150 m depth, associated with the detached patches of negative PV flow (Figure 1d). We also observe a low PV patch close to 300-m depth, which extends from the westbound seamount up to 40 km (see the deeper portion of T3 in Figure 2c) and contains points of inertial-symmetric hybrid instability. The deeper symmetric instability at 20–25 km, however, is not clearly linked to a low PV patch, and was probably classified as such due to very low stratification.

From the Ilhas summer survey data set, we observe several features, which hint at the BC and IWBC flows interacting with the VTR seamounts. At these sites, PV becomes negative and submesoscale instabilities may develop. Symmetric instabilities rise where constantly slanted isopycnals prevail close to topography. Also, our observations capture inertial instabilities that occur in seemingly pinched-off structures generated by the flow-topography interactions, as observed by D'Asaro (1988).

Next, we conduct a regional numerical experiment to further advance on the characterization of the submesoscale instabilities in the VTR region. In particular, we address the role of flow-topography interactions relatively to the snapshot obtained from the *Ilhas* summer cruise data set.

3. Submesoscale Permitting Simulations

A full characterization of the VTR's submesoscale activity requires high-resolution synoptic observations for different seasons, nonexistent in the region at present. Time series at selected locations along its nearly 1,000-km extension would also be necessary. Therefore, we opt to use the Regional Oceanic Modeling System (ROMS; Shchepetkin & McWilliams, 2005), employing a nested approach.

The parent grid spans from 41°16'S–62°34'W to 10°01'S–19°49'W, with 6 km of horizontal resolution and 30 vertical levels in terrain-following coordinates. We employed temperature and salinity fields from the Simple Ocean Data Assimilation (SODA) Project to initialize the simulation, forced by climatological monthly surface winds and heat fluxes from QuikSCAT and COADS, respectively. We run the simulation enforcing SODA fields as boundary conditions. This (parent) simulation was used in Napolitano et al. (2019), in which a thorough comparison of the model fields with observations of mesoscale features is presented.

The child grid resolution is 2 km, with 30 vertical levels in terrain-following coordinates, comprising the southeast Brazilian Margin (30°00'S–16°22'S, 50°16'W–25°07'W). Wind forcing and heat fluxes are the same used in the parent simulation, as well as *no* tidal forcing, which in turn allows a better separation of the submesoscale dynamics. To better resolve the complex topography of the VTR, the bathymetry resolution is about 4 km in the child grid, against 8 km of the parent grid. We used the past 5 years of the simulation in our analyses. In doing so, we interpolated the sigma-like vertical coordinates to standard depth levels, with a resolution of 2 m between 0 and 20 m, 5 m between 20 and 100 m, and 10 m between 100 and 200 m (the derived output was thus restricted to 200 m depth, with 36 fixed vertical grid levels). We emphasize that our goal in using the nested model is to obtain a submesoscale permitting simulation of the region, rather than a hindcast simulation of the observed transects.

As our quasisynoptic observations, our model horizontal resolution of 2 km and timescale of a few hours capture only the larger scale end of the submesoscale, which may permit submesoscale features to develop—see discussion surrounding Equations 3 and 4. We reinforce that the simulation cannot fully resolve symmetric instabilities, save only some modes of it, with lower growth rates (Bachman & Taylor, 2014). Moreover, with aspect ratio $\gg 1$, we acknowledge that gravitational instability also cannot be resolved: instead, the model allows convective adjustment. The term “gravitational instability” will thus refer to the model acting to restratify regions of $N^2 < 0$, using a KPP parameterization for vertical mixing.

The model resolution issue might account for an underestimation of the amount of unstable flow and the development of different types of instabilities. Idealized large eddy simulations (e.g., Stamper & Taylor, 2017; Thomas et al., 2013), and other submesoscale-modeling efforts (with horizontal grid resolution of hundreds of meters, for example, Gula et al., 2016; McWilliams et al., 2019), have highlighted some limita-

tions of coarser simulations such as our 2-km ROMS. On the contrary, a fully submesoscale-resolving resolution is prohibitive in a domain large enough to resolve the mesoscale western boundary currents, such as the BC and the IWBC. This stalemate will persist until computational resources allow large domains to be accommodated with the grid aspect ratio of unity.

3.1. Evaluation of the Submesoscale Dynamics in ROMS at 2 km Resolution

To investigate the development of submesoscale in our numerical simulation outputs, we use the full horizontal gradients of velocity and buoyancy. The diagnostics of submesoscale flows implies order $\mathcal{O}(1)$ rates of the nondimensional variables as

$$\text{vorticity} \stackrel{\text{def}}{=} \frac{\zeta}{|f|} = \frac{v_x - u_y}{|f|}, \quad (8)$$

$$\text{strain} \stackrel{\text{def}}{=} \frac{\alpha}{|f|} = \frac{\left[(u_x - v_y)^2 + (v_x + u_y)^2 \right]^{\frac{1}{2}}}{|f|}, \quad (9)$$

$$\text{divergence} \stackrel{\text{def}}{=} \frac{\delta}{|f|} = \frac{u_x + v_y}{|f|}, \text{ and} \quad (10)$$

$$\text{grad}b \stackrel{\text{def}}{=} \frac{M^2}{f^2} = \frac{|\nabla_h b|}{f^2}, \quad (11)$$

with Equations 8–10 usually associated with large lateral buoyancy gradients Equation 11. Detailed diagnostics for submesoscale flows can be found in Capet et al. (2007), Johnson et al. (2020), Mahadevan and Tandon (2006), Shcherbina et al. (2013), and Thomas et al. (2008).

Figure 3 (left panels) display snapshots of vorticity, strain, divergence, and gradb obtained from the 2-km ROMS simulation. We also computed the probability density function (PDF; see Figure 3, right panels) of the aforementioned rates within Tubarão Bight (the green square in the snapshots), following Shcherbina et al. (2013). We selected different days for each rate—which show the development of submesoscale-like features embedded in the mesoscale flow—and the corresponding PDFs, which present typical characteristics of submesoscale activity.

Figure 3a shows the PDF of vorticity. It presents large asymmetry, with a long tail toward cyclonic motions and skewness of -1.55 , which agrees with the results of Calil and Richards (2010), Molemaker et al. (2015), Rudnick (2001), and Shcherbina et al. (2013). The anticyclonic side of the vorticity PDF is restricted to order $\mathcal{O}(1)$ values, another signature of submesoscale activity (Mahadevan & Tandon, 2006).

The PDF of strain in Figure 3b follows a χ^2 distribution, with mean 0.28 and skew 2.02. A tail of sporadic high strain reveals extrema that are six times larger than the mean. Values of strain rate up to 2 are also reported by Rocha, Gille, et al. (2016) in daily-averaged model outputs, and by Johnson et al.'s (2020) observations. A skewed distribution is presented by Rocha, Gille, et al. (2016) and Shcherbina et al. (2013). In the ocean, such high strain rates intensify the lateral buoyancy gradients, leading to frontogenesis and larger vertical velocities (Mahadevan & Tandon, 2006).

Divergence rates in the PDF of Figure 3c reveals order $\mathcal{O}(1)$ values, with a slightly skewed distribution toward convergence. This asymmetry is typical of submesoscale, associated with frontal sharpening and downwelling (McWilliams et al., 2009). Our PDF distribution is consistent with the model results of Pérez and Calil (2017) for the Equatorial Atlantic, and observations reported by Johnson et al. (2020) off the California coast. A high-resolution theoretical simulation by McWilliams et al. (2019) shows order $\mathcal{O}(1)$ divergence accompanying a mesoscale meander, associated with large vertical velocities [$\mathcal{O}(10^{-3}) \text{ ms}^{-1}$].

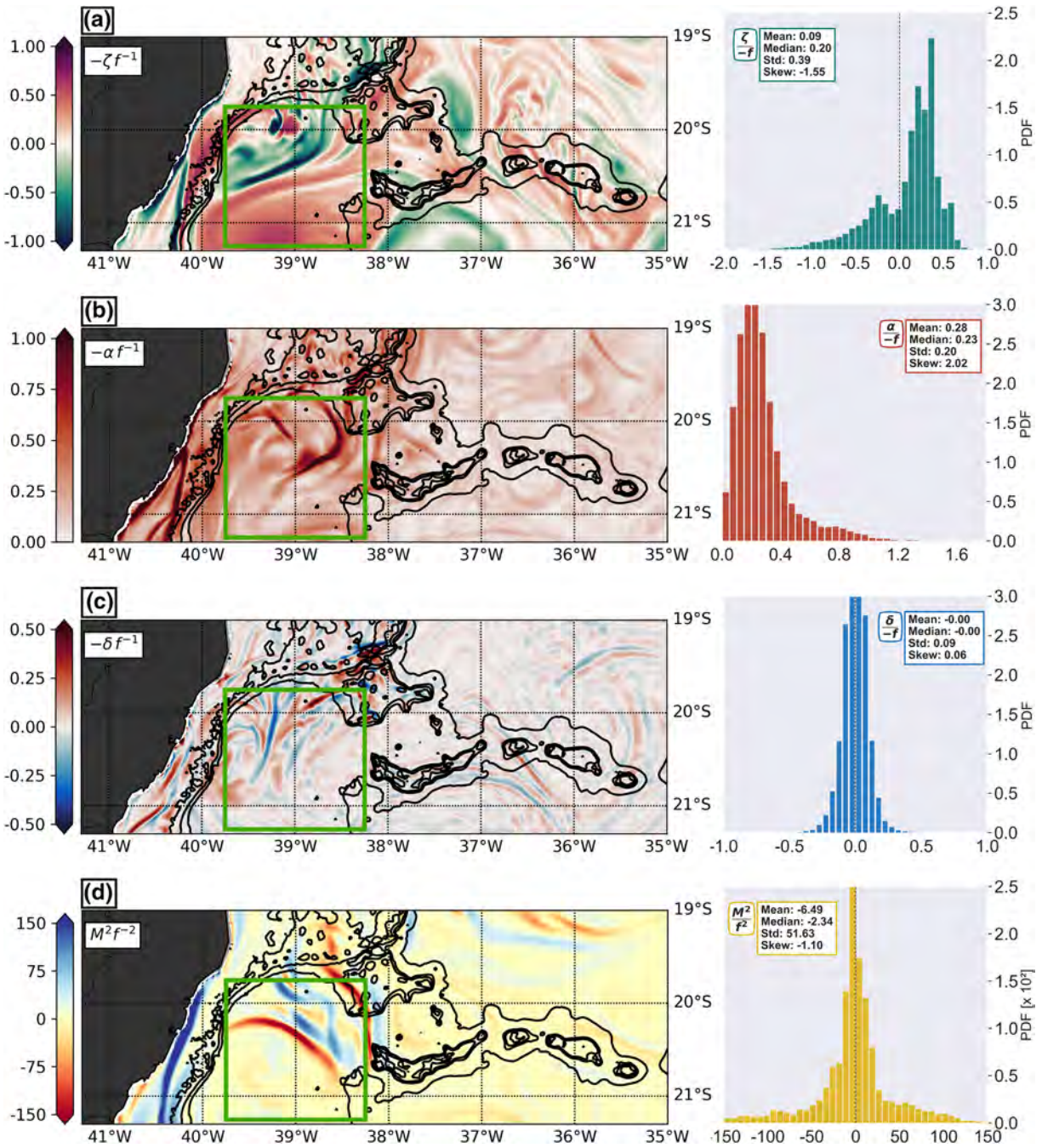


Figure 3. Snapshots and probability density functions (PDFs) of the 2-km ROMS simulation at the surface, showing rates of (a) relative vorticity $-\zeta/f$, (b) strain $-\alpha/f$, (c) divergence $-\delta/f$, and (d) lateral buoyancy gradient M^2/f^2 . The PDFs are computed within the green box shown in the snapshots.

However, our simulation results differ from the North Atlantic, open ocean, winter observations of Shcherbina et al. (2013), who found larger values (~ 1.5) and a more skewed distribution (0.20).

In Figure 3d, the PDF of gradb shows a nearly symmetric distribution, with a large standard deviation of 51.63. We observe that strong fronts of buoyancy, with magnitude $4 \times 10^{-7} \text{ s}^{-2}$, are responsible for these large deviations. In a review of the submesoscale processes, Mahadevan (2016) points out that lateral buoyancy gradients of 10^{-7} s^{-2} yield horizontal length scales of 1 km. Submesoscale idealized simulations by Thomas et al. (2016) and Wenegrat et al. (2018) use buoyancy gradients at fronts to about $5 \times 10^{-7} \text{ s}^{-2}$. Strong fronts observed by Johnson et al. (2020) reveal high gradb of about 200. A higher-resolution model of a Gulf

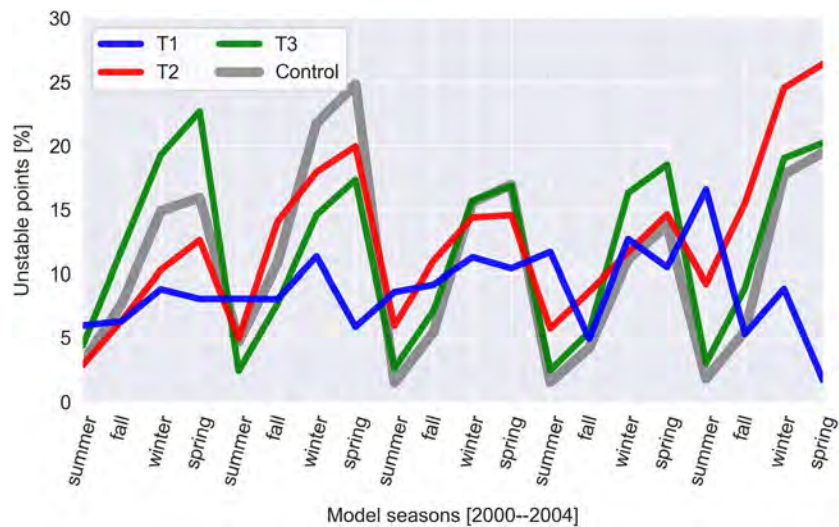


Figure 4. Model timeseries of the percentage of unstable points (i.e., $PV < 0$) for T1 (blue), T2 (red), and T3 (green). The gray thick line represents a control transect obtained upstream of the study region, away from the influence of topography.

Stream meander, presented by McWilliams et al. (2019), shows lateral buoyancy gradients of about 10^{-6}s^{-2} , therefore, half-order of magnitude larger than our 2-km ROMS values.

The rates presented in Figure 3 show that these model values are consistent with other numerical studies and recent observations, and adequate to characterize submesoscale phenomena. In a region with rough topography such as the VTR, locally excited internal waves likely interact with the submesoscale and topography (Whalen et al., 2020; Whitt et al., 2018), affecting the diagnostic rates. We observe weaker magnitude and substantial intermittency of the submesoscale motions throughout the model timeseries. The intermittent character of these motions seems intrinsic to how submesoscale manifest in the ocean (Capet et al., 2007).

3.2. Seasonal Characterization

Traditionally, seasonality in submesoscale flows has been related to the mixed-layer seasonal cycle. A deep, energetic mixed layer in winter presents more submesoscale activity than that of a shallow and stratified summer mixed layer (e.g., Calil, 2017; Callies et al., 2015; Mensa et al., 2013; Sasaki et al., 2014). In the Gulf Stream region, Mensa et al. (2013) showed a clear seasonal cycle in submesoscale comparing two numerical simulations of different horizontal resolutions. Later, Callies et al. (2015) confirmed this seasonality, reporting observations in winter and summertime. High-resolution numerical simulations have all but confirmed the enhanced submesoscale activity in the wintertime in the open ocean, primarily due to buoyancy loss and increased winds over frontal regions (Calil, 2017; Sasaki et al., 2014).

To assess the submesoscale seasonality in the BC–IWBC domain of our simulation, first we extract the blowout regions of the observed transects (T1–T3) from the model outputs (see Figures 2d–2f); second, we calculate the Ertel PV Equation 5) for the upper 200 m of the water column. When compared with a control transect upstream of the seamount region, the percentage of unstable points (grid points with $PV < 0$, Figure 4) in T3, the less influenced by the BC and topography, follows the typical mixed-layer seasonal cycle. On average, 3% of T3 is unstable in summer, increasing in fall to about 8%. This percentage peaks in winter and spring, representing 17% and 19% of the transect, respectively. Our results are consistent with recent studies of submesoscale seasonality in the Kuroshio Extension, which report early spring peaks (cf. Rocha, Gille, et al., 2016; Sasaki et al., 2017). T2 shows a slight increase in the percentage of unstable flow in summer, from 3% to 6%, and in fall from 8% to 11%. But the mixed-layer seasonal cycle still dominates the distribution of unstable points in the transect, with higher values in winter (16%) and spring (18%).

In T1, however, the occurrence of unstable flow in Figure 4 diverges from the seasonal patterns of T2 and T3. This is the region where the BC flow strikes off through the seamounts (see also observations in Figure 1 and model snapshots in Figure 3). The percentage of unstable flow cycles from 10% to 7% from summer to fall, as well as from winter to spring. Although different factors may affect seasonality, the close location between the transects, as well as the constant seasonal winds in the region, would not alone explain such seasonal differences. In our model, forcing was relatively uniform over the region in focus, so it is unlikely that this is the cause of the different dynamics reported. The smaller amount of unstable points in T1 is due to the influence of the BC, which reduces the depth of the mixed layer (Calado et al., 2010), where most of the instabilities occur. But the BC also presents a seasonal cycle (e.g., Schmid & Majumder, 2018), suggesting that the absence of a clear seasonal cycle in T1 results from the interaction between the western boundary currents and the topography. Such interaction may generate unstable flow throughout the year, destabilizing the water column and leading to filamentation, eddy formation, and the triggering of internal lee waves through instability processes.

3.3. Flow-Topography Interactions

Vertical fluxes of buoyancy are telltale of an ongoing instability process. Here, we define a buoyancy flux anomaly as the deviation from a slowly varying vertical buoyancy flux, through the decomposition of the model outputs:

$$wb = \overline{wb} + (wb)'. \quad (12)$$

The daily term $(wb)'$ in Equation 12, associated with submesoscale, is the deviation from a low-pass filtered mean $(\overline{\quad})$ of 3 days, equivalent to two times the inertial period. Anomalies from a mean vertical buoyancy flux $(wb)' < 0$ indicate that a water parcel is displaced from its average, stable depth. These unstable conditions lead to instabilities (or equivalent model responses) that act to restratify the water column, which in turn yield $(wb)' > 0$. This destabilization-restratification cycle is recurrent throughout the model timeseries.

We then define an even slower varying submesoscale buoyancy flux $(\overline{wb'})$ of 6 days, hereon SBF, which corresponds approximately to a full destabilization–restratification cycle.

Figure 5 explores the spatiotemporal variability of the SBF in the model. Figures 5a–5c show the time evolution of the along-transect averaged SBF for T1, T2, and T3, respectively. Also, they show the tendency of the MLD and the isopycnal $\rho = 1,025.9 \text{ kgm}^{-3}$ (hereafter 25.9), which marks the interface between the warmer surface waters and the colder, nutrient-rich waters occupying the pycnocline (cf. Lazaneo et al., 2020). From the full model timeseries, we observe that all transects show a mixed-layer seasonal cycle. Nevertheless, this cycle is much more pronounced in T3 than in T1 or T2. Given the proximity between the transects, this difference can only be attributed to the presence of the BC in T1 and T2. This weakened seasonal effect appears to be related to the BC baroclinic geostrophic adjustment, which lifts the pycnocline (e.g., Calado et al., 2010), with upper pycnocline waters observed at 150 m within Tubarão Bight (e.g., Costa et al., 2017).

Figures 5a–5c show strong positive SBF associated with the thickness of the mixed (convective) layer (Taylor & Ferrari, 2010) and consistent with that of Thomas et al. (2016). Below the MLD, patterns of SBF greatly differ. In transect T1, instabilities also develop between the MLD and the 25.9 isopycnal, with stronger SBF around 150 m. Even deeper unstable conditions are observed in transect T2, where the strongest SBF occurs below the 25.9 isopycnal (Figure 5b). In transect T3, however, unstable conditions develop almost solely within the mixed layer (Figure 5c).

Analyzing vertical snapshots of SBF, we identify two regimes: one clearly associated with mixed-layer dynamics (e.g., T3) and a second associated with flow-topography interactions (e.g., T1). As a consequence of the destabilization-restratification process, the submesoscale vertical fluxes move isopycnals up and down the water column. The right panels of Figure 5 detail periods of strong SBF and the resulting vertical displacements of the 25.9 isopycnal. Additionally, snapshots of each transect when SBF is the strongest show the spatial distribution of the instabilities (Figure 6).

Figures 5d–5f compare the 25.9 isopycnal to a mean (6 days averaged) isopycnal $\overline{\rho} = 25.9 \text{ kgm}^{-3}$. The time-mean $\overline{\rho}$ averages out the effects of submesoscale destabilization and restratification, dampening the varia-

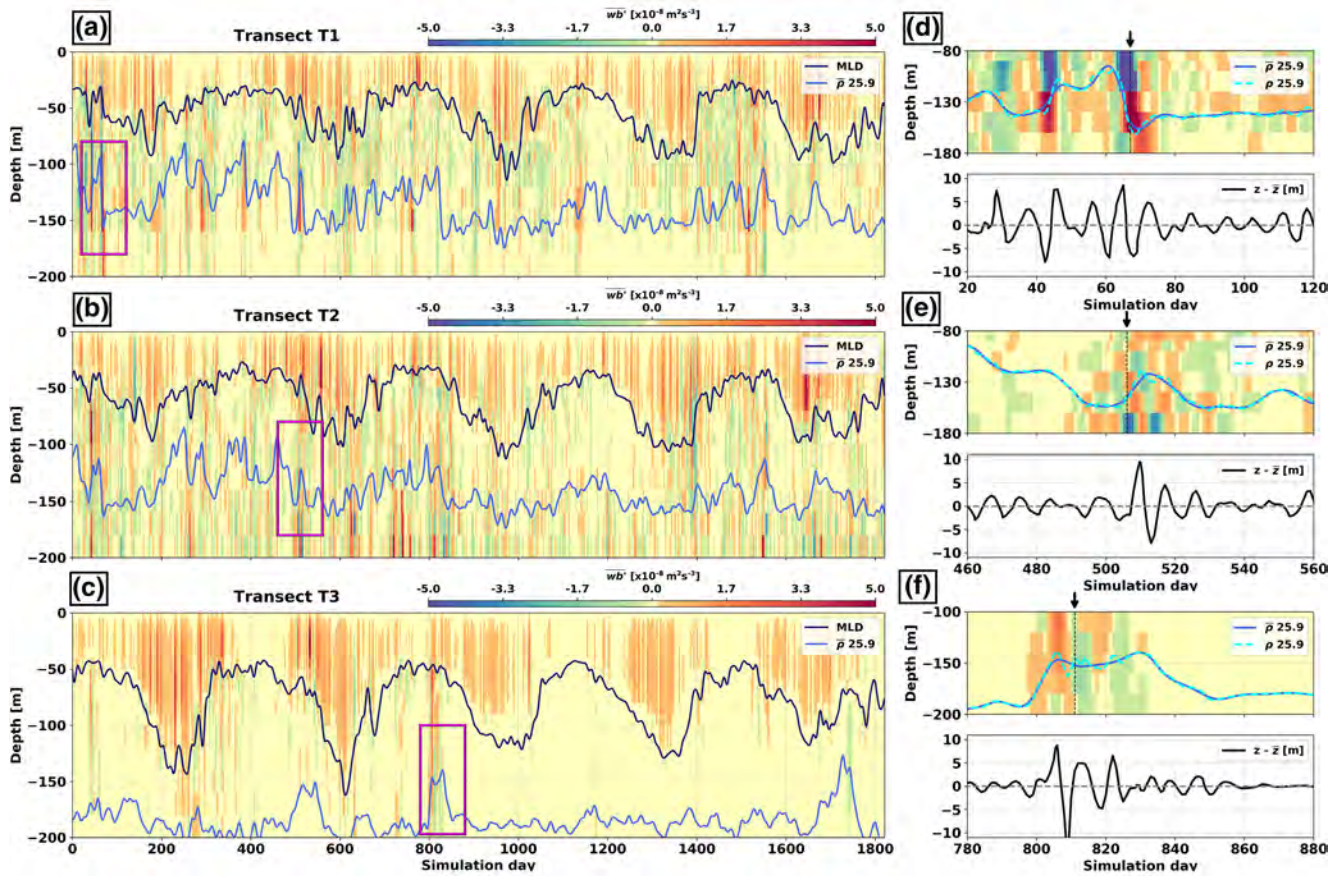


Figure 5. Left: model timeseries of the along-transect averaged SBF ($\overline{wb'}$) for T1 (a), T2 (b), and T3 (c). The dark blue line represents the MLD, and the light blue line represents the $\bar{\rho} = 1025.9 \text{ kgm}^{-3}$ isopycnal. The magenta boxes indicate periods of strong SBF events affecting $\bar{\rho}$. Right: blowout of strong SBF events within the model timeseries for T1 (d), T2 (e), and T3 (f). The cyan line represents the $\rho = 1,025.9 \text{ kgm}^{-3}$ isopycnal. The blue line represents the 6-day mean $\bar{\rho} = 1025.9 \text{ kgm}^{-3}$ isopycnal. The black line in the lower panels represents the depth difference between the isopycnal ρ and the mean isopycnal $\bar{\rho}$. The arrow and dashed line indicate 1 day of simulation with strong SBF.

tions in the 25.9 isopycnal. Therefore, while crossing regions of strong SBF, the curves instantly diverge. To track the daily changes in the depth of the 25.9 isopycnal, we simply subtract it from the depth of the mean isopycnal. Due to vertical motions induced by submesoscale processes, in our simulation, the difference $z - \bar{z}$ reaches about 20 mday^{-1} , fluctuating $\sim 0.04 \text{ kgm}^{-3}$ around the mean isopycnal. Close to this depth range, Legal et al. (2007) obtained similar values for 0.05 kgm^{-3} density anomalies within elongated, filament-like structures.

The PV snapshots at 140 m (Figures 6a–6c), during a high-SBF event (identified by the arrows in Figures 5d–5f), show potentially unstable conditions developing close to topography in T1 and T2. Some low-PV patches appear close to T3, but no negative-PV contours are identified. These unstable conditions constantly appear next to topography throughout the model simulation, and are likely to set the destabilization-restratification cycle observed in the timeseries. The vertical sections associated with the strongest SBF (Figures 6d–6f) show that SBF peaks near topographic features. The intermittent peaks in the T1 timeseries (Figures 5a and 5d) clearly coincide with the depth range where the flow rubs against topography in Figures 6a and 6d. A similar pattern is seen in T2 (see the high SBF in the lower right of Figures 6b and 6e). The flow in T3, which is more akin to an open ocean condition—as there is no direct interaction with the topography—has a more homogeneous distribution, showing no negative PV nor a distinct peak in Figures 6c and 6f.

At the VTR region, flow-topography interactions are likely to play a major role in generating submesoscale instabilities. In a frontal region, Martin et al. (2001) reported strong vertical velocities of $\mathcal{O}(10) \text{ mday}^{-1}$, as-

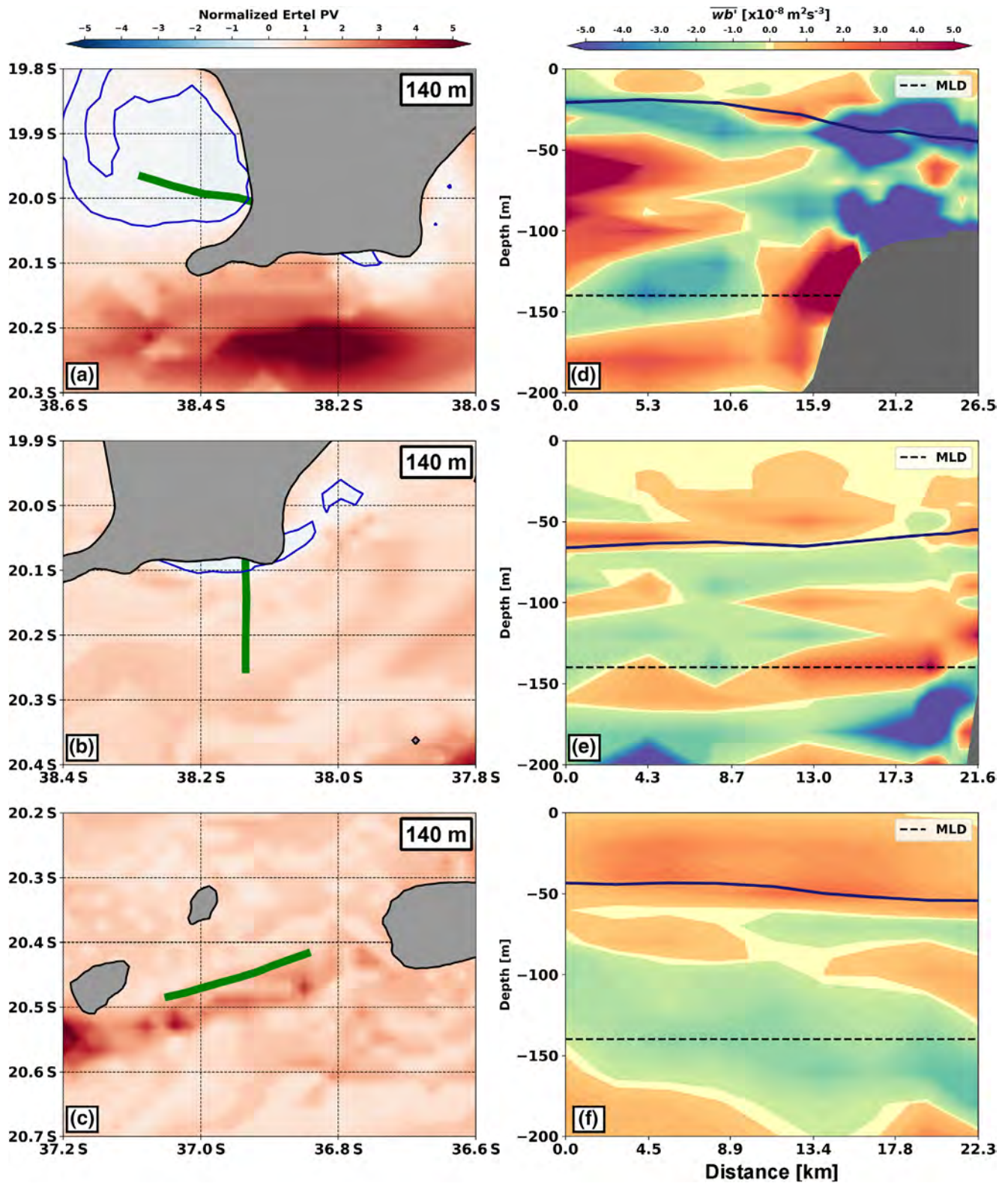


Figure 6. Horizontal distribution of potential vorticity at 140 m for the region around the transects, on (a) model day 67 for T1, (b) 506 for T2, and (c) 811 for T3. The vertical distribution of the submesoscale buoyancy flux for the corresponding days is shown in panels (d), T1, (e), T2, and (f), T3.

sociated with ageostrophic secondary circulations, which drive productivity blooms in oligotrophic regions, as nutrients and organisms are exposed to increasing light levels. In this context, Mahadevan (2016) also showed that rapid changes in the depth of isopycnals are key to control primary production. Downward variations are also important, leading to submesoscale subduction, potentially enhancing the carbon sink through slanted isopycnals (Mahadevan, 2016; Omand et al., 2015). To further investigate the effects of the BC interacting with topography, we evaluate the unstable $PV < 0$ flow throughout the model timeseries. At each transect, we calculate the $\tan(\phi_{Rib}) = -Ri_B^{-1}$ angle presented in Equation 1 to classify, considering the model limitations, the regions and seasons prone to different instabilities, analogously to what we performed in Section 2 for the observations.

3.4. Instability Types

Along with the percentage of negative PV, instability types may change seasonally. In general, stable conditions in summer develop into unstable stratification in fall; a deeper mixed layer in winter, and restratification in early spring, favor symmetric instability (e.g., Thompson et al., 2016). Also, spatial heterogeneity can result in abrupt changes in the submesoscale instability types (e.g., Viglione et al., 2018). As already discussed above, both temporal and spatial variability of the flow across the VTR, that is, the mixed-layer seasonal cycle and the interaction between the BC and the seamounts, are likely to play a role in determining the types of instability.

In Figure 7, we adapted Thomas' diagrams to display not only the type of instability which the flow develops (shown azimuthally), but also the depth at which these instabilities occur (shown radially). The schematic diagram in the upper left of Figure 7 shows the instability types related to the angle ϕ_{Rib} . To build the seasonal diagrams, we first computed the total amount of unstable flow at each grid point for T1–T3 for every season of the ROMS timeseries. Second, we classified the instabilities following Thomas et al. (2013), with their percentage displayed in the corresponding diagram slices. Colors show the PDF of ϕ_{Rib} , normalized at every depth by the maximum PDF value. This normalization excludes the stable low PV region.

Figure 7 presents the Thomas diagrams for flow with anticyclonic vorticity on T1–T3. As previously discussed, T3 (at the outer channel) presents the deepest mixed layer in all seasons and undergoes a standard seasonal evolution, with higher submesoscale activity in winter and spring. Gravitational instability represents about 40% of the negative PV throughout 5 years of simulation. Modes of symmetric instabilities and their hybrid forms (symmetric-gravitational and symmetric-inertial) increase as the mixed layer deepens, responding for about 30% of the instabilities in winter and spring. Symmetric instabilities in T3 seldom occur below the MLD.

The percentage of unstable flow in T1 south of Abrolhos Bank does not follow the seasonal cycle of the MLD. But a portion of the 57% stable $PV < 0$ in summer is classified as gravitationally unstable in fall (an increase from 29%–42%), typical of the erosion process of the mixed layer. Thus, other types of instabilities drive the changes in the amount of negative PV in this transect, which do not follow the standard mixed-layer cycle. As in T3, mixed gravitational–symmetric instabilities are about 12% from fall to spring. The resolved modes of symmetric and symmetric-inertial instabilities represent 5% of the unstable flow, independently of season. These instabilities generally peak below the MLD, dominating the unstable flow below 100 m.

We discuss T2 last, as it presents characteristics in between T3 and T1. In the main channel, T2 shows a distribution of instabilities comparable to T3 in summer, with instabilities restricted to the mixed layer. Here, the percentage of gravitational instability also remains nearly constant throughout the year, accounting for about 45% of the negative PV. But from fall to spring, the T2 diagrams present a pattern similar to that of T1. Symmetric instabilities represent only 2% of the unstable flow, but occur mostly below the MLD. The observations depict symmetric instability developing from the interaction of the IWBC and a seamount; in ROMS, a smoothed topography and deeper IWBC may result in deeper instabilities, not fully captured by our 200-m depth transect. We observe no inertial instabilities in T2.

The transition of the instability types occurring below the MLD seen from T3 to T1 follows the influence of topography. Although we do not observe an abrupt transition in the types of instabilities as those in Viglione

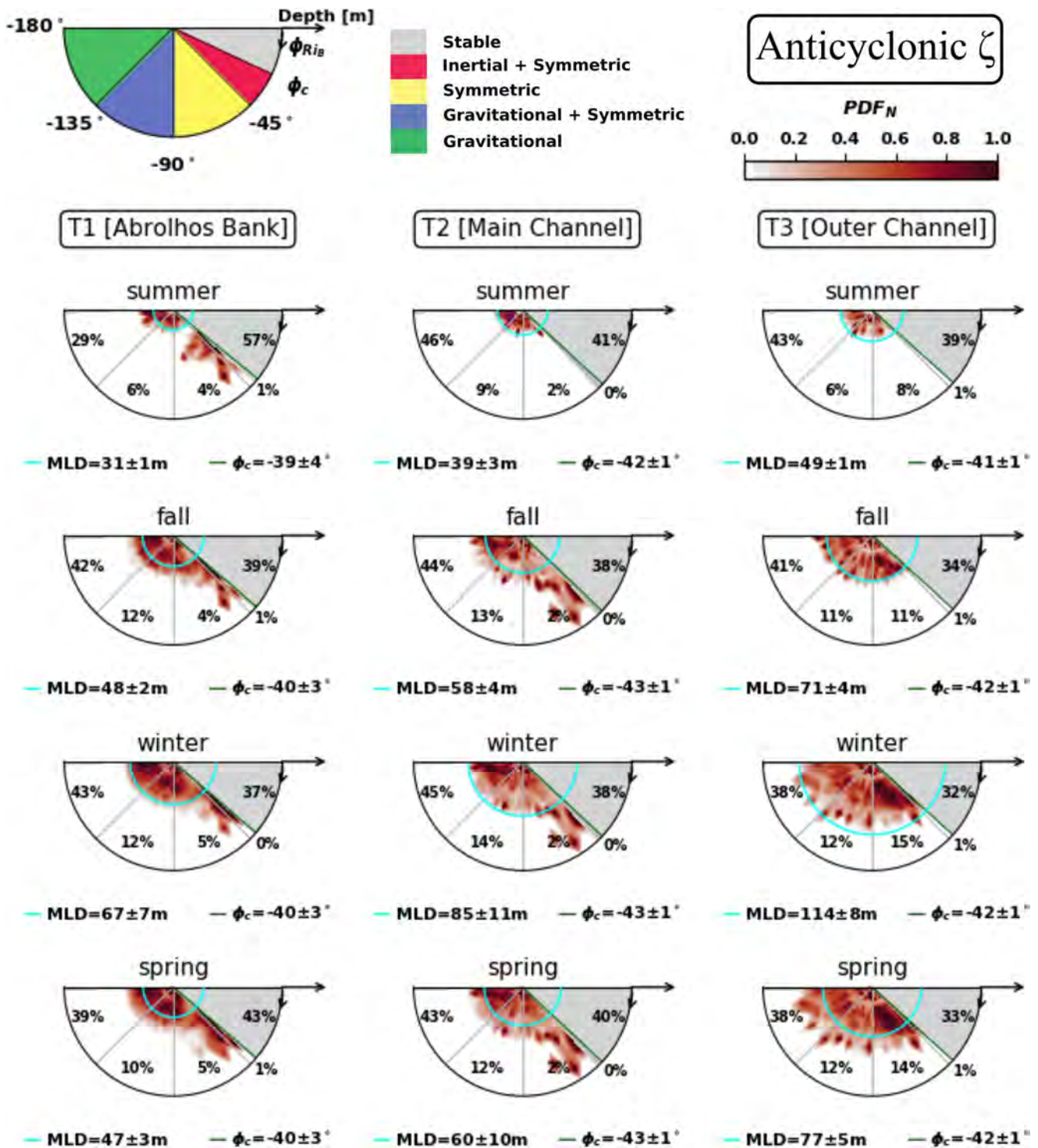


Figure 7. The adapted Thomas' diagrams for the classification of the instabilities for flow with *anticyclonic vorticity*, by type and depth, for transects T1–T3 of the ROMS simulation. The azimuth ϕ_{RIB} denotes the instability type, while the radial distance indicates the depth in which each instability type is identified. For every season, the slices of the diagram contain the average percentage of their corresponding instability type. Colors show the PDF of ϕ_{RIB} , normalized at every depth by the maximum PDF value, not considering the gray-shaded, stable low PV. For better visualization, the depth axis is restricted to 170 m. The cyan line represents the mean mixed-layer depth (MLD) for the season. The green lines delimit the region between -45° and the critical angle ϕ_c .

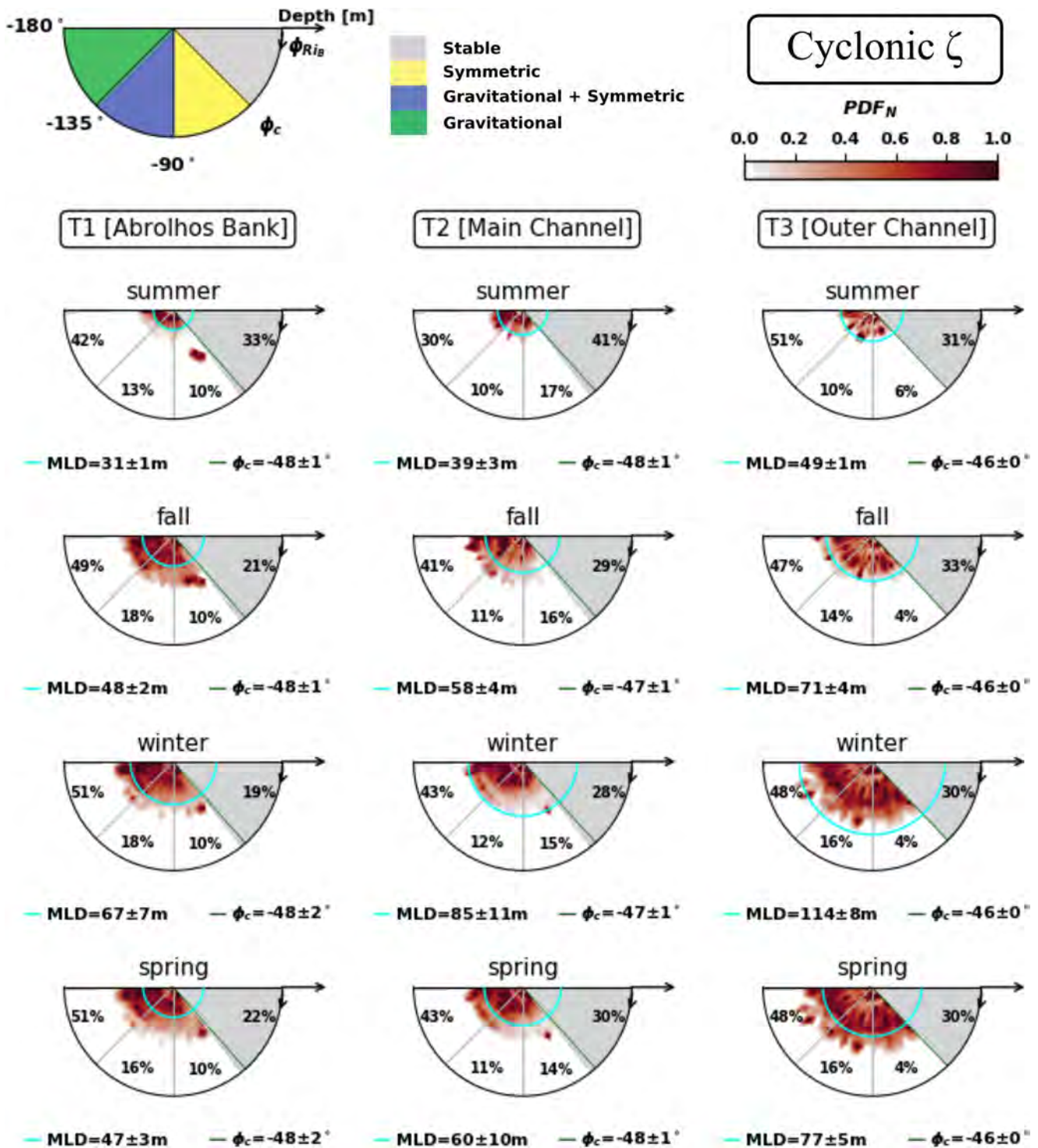


Figure 8. The adapted Thomas diagrams for the classification of the instabilities for flow with *cyclonic vorticity*, by type and depth, for transects T1–T3 of the ROMS simulation. The azimuth ϕ_{Rib} denotes the instability type, while the radial distance indicates the depth at which each instability type is identified. For every season, the slices of the diagram contain the average percentage of their corresponding instability type. Colors show the PDF of ϕ_{Rib} , normalized at every depth by the maximum PDF value, not considering the gray-shaded, stable low PV. For better visualization, the depth axis is restricted to 170 m. The cyan line represents the mean MLD for the season. The green lines delimit the region between -90° and the critical angle ϕ_c .

et al. (2018), instabilities due to flow-topography interactions represent nearly all deep symmetric instabilities. Some of these occur in isolated patches, much deeper than the MLD. Even with coarse resolution and only partially resolving submesoscale instabilities, our simulation shows the importance of flow-topography interactions in generating such instability modes.

Flow with cyclonic vorticity presents a similar pattern for the three transects (Figure 8). As in T3 for anticyclonic vorticity, instabilities occur mostly within the mixed layer. When compared with anticyclonic-vorticity diagrams, the percentage of stable $PV < 0$ decreases about 10%. Curiously, symmetric instability (plus its hybrids) presents an opposite pattern: in T1 and T2, they represent about 30% of the unstable flow, whereas in T3 they account for about 4%. Cyclonic-vorticity flow instabilities seldom occur below the mixed layer, except for small patches of symmetric instabilities in T1.

4. Final Remarks

The VTR region plays an important role in the dynamics of the western boundary current system off Eastern Brazil. Costa et al. (2017) showed that the IWBC crosses the VTR forming a quasistationary recirculation, which occupies Tubarão Bight at intermediate levels. The interaction of the jet, the recirculation, and westward-propagating nonlinear waves cause advection and downstream perturbation growth, as they negotiate the main and outer channels (Napolitano et al., 2019). In the upper layers, the BC crosses the VTR forming a large cyclonic loop, occasionally forming the Vitória Eddy (Schmid et al., 1995), and reattaches to the continental margin south of 21°S (Lazaneo et al., 2020). Hence, the mesoscale activity of the western boundary currents is already set up in those studies, but not the submesoscale phenomena associated with them. This study aims to present a first glimpse of the submesoscale dynamics set off by these currents as they cross the VTR, or in other words, their interaction with the topography of the ridge's seamounts.

Three transects of shipboard-ADCP velocity and underway-CTD-derived density in the region captures the first submesoscale features ever observed at the VTR region, associated with the BC and the IWBC negotiating the ridge's complex topography. We analyzed low PV patches in the transects, each one presenting a different level of interaction between the flow and topography. While gravitational instabilities dominate the negative PV close to the base of the mixed layer, symmetric and the hybrids symmetric-gravitational and symmetric-inertial instabilities appear at unstable regions where the western boundary currents rub against the seamounts. Moreover, inertial instabilities dominate observed submesoscale eddies, which are likely formed due to topographic steering of the flow.

Using a submesoscale-motion permitting regional numerical simulation, we show that seasonal variations are important in the generation of negative PV at the VTR. But spatial differences, characterized by the presence of topography, impose important changes in the seasonality of the modeled transects. These two distinct regimes influence the distribution of instabilities and may interact with each other when a deeper mixed layer intersects the seamounts topography. Away from topography, transect T3 exhibits a typical seasonal cycle of submesoscale, with instabilities developing within the mixed layer. Transect T2 reveals deep symmetric instabilities (>150 m) developing below the mixed layer, with intermittent peaks close to 200-m depth, where the flow encounters topography. Symmetric instabilities frequently occur below the mixed layer in transect T1, where a prominent seamount constantly interacts with the BC. There, flow-topography interactions mask the seasonality of submesoscale dynamics, showing no clear cycle in the amount of unstable flow throughout the years.

In the VTR region, topographically driven instabilities appear as an important mechanism that displaces pycnocline isopycnals by several meters. These upwelled isopycnals expose nutrient-rich waters to different sunlight and may boost primary productivity below the mixed layer. As a counterpart effect, subducted isopycnals may fuel the carbon pump, driving particles and organisms away from sunlit regions.

Finer-resolution simulations than the 2 km grid employed in this work are already under development for future studies in the region. These simulations also include a version with tides, which aim to better separate effects of internal waves from submesoscale motions, which were not addressed in the present discussion. However, the lack of observations still remains as the main obstacle to better understand the

submesoscale processes linked to the BC–IWBC system and the VTR, and how they change the dynamics up- and downstream the ridge.

Data Availability Statement

The data used in this study can be obtained at <https://jmp.sh/ciSdvkG>.

Acknowledgments

The authors thank Cauê Z. Lazaneo for the help in the numerical model assessment. D. C. Napolitano acknowledges support from Coordenação de Aperfeiçoamento de Pessoal de Nível Superior (CAPES)–Finance Code 001 and Projeto Santos (Petrobras 3368). I. C. A. da Silveira acknowledges support from CNPq (Grant 307814/2017-3), Projeto SUBMESO (CNPq 442926/2015-4), Projeto REMARSUL (CAPES 88882.158621/2014-01), and Projeto VT-Dyn (FAPESP 2015/21729-4). A. Tandon acknowledges support from the Office of Naval Research (Grant N000141812799) and the National Science Foundation (OCE-1755313). P. H. R. Calil acknowledges support from CNPq (Grant 306971/2016-0) and Projeto ILHAS (CNPq 458583/2013-8).

References

- Arruda, W. Z., & Silveira, I. C. A. (2019). Dipole-induced central water extrusions South of Abrolhos Bank (Brazil, 20.5S). *Continental Shelf Research*, 188, 103976. <https://doi.org/10.1016/j.csr.2019.103976>
- Bachman, S. D., Fox-Kemper, B., Taylor, J. R., & Thomas, L. N. (2017). Parameterization of frontal symmetric instabilities. I: Theory for resolved fronts. *Ocean Modelling*, 109, 72–95.
- Bachman, S. D., & Taylor, J. R. (2014). Modelling of partially-resolved oceanic symmetric instability. *Ocean Modelling*, 82, 15–27.
- Benthuyzen, J., & Thomas, L. N. (2012). Friction and diapycnal mixing at a slope: Boundary control of potential vorticity. *Journal of Physical Oceanography*, 42(9), 1509–1523.
- Boccaletti, G., Ferrari, R., & Fox-Kemper, B. (2007). Mixed layer instabilities and restratification. *Journal of Physical Oceanography*, 37(9), 2228–2250. <https://doi.org/10.1175/JPO3101.1>
- Calado, L., Silveira, I. C. A., Gangopadhyay, A., & Castro, B. M. (2010). Eddy-induced upwelling off Cape São Tomé (22 S, Brazil). *Continental Shelf Research*, 30(10–11), 1181–1188.
- Calil, P. H. R. (2017). Wind-induced subduction at the South Atlantic subtropical front. *Ocean Dynamics*, 67(10), 1351–1365. <https://doi.org/10.1007/s10236-017-1090-z>
- Calil, P. H. R., & Richards, K. J. (2010). Transient upwelling hot spots in the oligotrophic North Pacific. *Journal of Geophysical Research*, 115(C2). <https://doi.org/10.1029/2009JC005360>
- Callies, J., Ferrari, R., Klymak, J. M., & Gula, J. (2015). Seasonality in submesoscale turbulence. *Nature Communications*, 6(1), 1–8.
- Capet, X., McWilliams, J. C., Molemaker, M. J., & Shchepetkin, A. F. (2007). Mesoscale to submesoscale transition in the California current system. Part I: Flow structure, eddy flux, and observational tests. *Journal of Physical Oceanography*, 38(1), 29–43. <https://doi.org/10.1175/2007JPO3671.1>
- Capet, X., McWilliams, J. C., Molemaker, M. J., & Shchepetkin, A. F. (2008). Mesoscale to submesoscale transition in the California current system. Part III: Energy balance and flux. *Journal of Physical Oceanography*, 38(10), 2256–2269. <https://doi.org/10.1175/2008JPO3810.1>
- Costa, V. S., Mill, G. N., Gabioux, M., Grossmann-Matheson, G. S., & Paiva, A. M. (2017). The recirculation of the intermediate western boundary current at the Tubarão Bight–Brazil. *Deep Sea Research Part I: Oceanographic Research Papers*, 120, 48–60.
- D’Asaro, E. A. (1988). Generation of submesoscale vortices: A new mechanism. *Journal of Geophysical Research*, 93(C6), 6685–6693.
- D’Asaro, E. A., Lee, C., Rainville, L., Harcourt, R., & Thomas, L. (2011). Enhanced turbulence and energy dissipation at ocean fronts. *Science*, 332(6027), 318–322.
- Evans, D. L., Signorini, S. R., & Miranda, L. B. (1983). A note on the Transport of the Brazil current. *Journal of Physical Oceanography*, 13(9), 1732–1738. <https://doi.org/10.1175/1520-0485>
- Firing, E., Ranada, J., & Caldwell, P. (1995). *Processing ADCP data with the CODAS software system version 3.1*. Bremerhaven, Germany: Joint Institute for Marine and Atmospheric Research, University of Hawaii & National Oceanographic Data Center.
- Fox-Kemper, B., Ferrari, R., & Hallberg, R. (2008). Parameterization of mixed layer eddies. Part I: Theory and diagnosis. *Journal of Physical Oceanography*, 38(6), 1145–1165. <https://doi.org/10.1175/2007JPO3792.1>
- Gula, J., Molemaker, M. J., & McWilliams, J. C. (2016). Topographic generation of submesoscale centrifugal instability and energy dissipation. *Nature Communications*, 7, 12811.
- Johnson, L., Lee, C. M., D’Asaro, E. A., Thomas, L., & Scherbina, A. (2020). Restratification at a California current upwelling front, Part 1: Observations. *Journal of Physical Oceanography*, 50, 1455–1472. <https://doi.org/10.1175/JPO-D-19-0203.1>
- Klein, P., Treguier, A.-M., & Hua, B. L. (1998). Three-dimensional stirring of thermohaline fronts. *Journal of Marine Research*, 56(3), 589–612.
- Lazaneo, C. Z., Napolitano, D. C., Silveira, I. C. A., Tandon, A., MacDonald, D. G., Ávila, R. A., & Calil, P. H. R. (2020). On the role of turbulent mixing produced by vertical shear between the Brazil Current and the Intermediate Western Boundary Current. *Journal of Geophysical Research: Oceans*, 125, e2019JC015338. <https://doi.org/10.1029/2019JC015338>
- Legal, C., Klein, P., Treguier, A.-M., & Paillet, J. (2007). Diagnosis of the vertical motions in a mesoscale stirring region. *Journal of Physical Oceanography*, 37(5), 1413–1424.
- Legeais, J.-F., Ollitrault, M., & Arhan, M. (2013). Lagrangian observations in the intermediate western boundary current of the South Atlantic. *Deep Sea Research Part II: Topical Studies in Oceanography*, 85, 109–126. <https://doi.org/10.1016/j.dsr2.2012.07.028>
- Lévy, M., Ferrari, R., Franks, P. J., Martin, A. P., & Rivière, P. (2012). Bringing physics to life at the submesoscale. *Geophysical Research Letters*, 39(14). <https://doi.org/10.1029/2012GL052756>
- Lueck, R. G., & Mudge, T. D. (1997). Topographically induced mixing around a shallow seamount. *Science*, 276(5320), 1831–1833.
- Mahadevan, A. (2016). The impact of submesoscale physics on primary productivity of plankton. *Annual Review of Marine Science*, 8, 161–184.
- Mahadevan, A., & Archer, D. (2000). Modeling the impact of fronts and mesoscale circulation on the nutrient supply and biogeochemistry of the upper ocean. *Journal of Geophysical Research*, 105(C1), 1209–1225.
- Mahadevan, A., & Tandon, A. (2006). An analysis of mechanisms for submesoscale vertical motion at ocean fronts. *Ocean Modelling*, 14(3–4), 241–256.
- Mano, M. F., Paiva, A. M., Torres, A. R., & Coutinho, A. L. G. A. (2009). Energy flux to a cyclonic eddy off Cabo Frio, Brazil. *Journal of Physical Oceanography*, 39(11), 2999–3010. <https://doi.org/10.1175/2009JPO4026.1>
- Martin, A. P., Richards, K. J., & Fasham, M. J. R. (2001). Phytoplankton production and community structure in an unstable frontal region. *Journal of Marine Systems*, 28(1–2), 65–89.

- McWilliams, J. C. (1985). Submesoscale, coherent vortices in the ocean. *Reviews of Geophysics*, 23(2), 165–182. <https://doi.org/10.1029/RG023i002p00165>
- McWilliams, J. C. (2016). Submesoscale currents in the ocean. *Proceedings of the Royal Society A: Mathematical, Physical and Engineering Sciences*, 472(2189), 20160117.
- McWilliams, J. C., Colas, F., & Molemaker, M. J. (2009). Cold filamentary intensification and oceanic surface convergence lines. *Geophysical Research Letters*, 36(18). <https://doi.org/10.1029/2009GL039402>
- McWilliams, J. C., Gula, J., & Molemaker, M. J. (2019). The gulf stream north wall: Ageostrophic circulation and frontogenesis. *Journal of Physical Oceanography*, 49(4), 893–916.
- Mensa, J. A., Garraffo, Z., Griffa, A., Özgökmen, T. M., Haza, A., & Veneziani, M. (2013). Seasonality of the submesoscale dynamics in the gulf stream region. *Ocean Dynamics*, 63(8), 923–941.
- Molemaker, M. J., McWilliams, J. C., & Capet, X. (2010). Balanced and unbalanced routes to dissipation in an equilibrated eady flow. *Journal of Fluid Mechanics*, 654, 35–63. <https://doi.org/10.1017/S0022112009993272>
- Molemaker, M. J., McWilliams, J. C., & Dewar, W. K. (2015). Submesoscale instability and generation of mesoscale anticyclones near a separation of the California undercurrent. *Journal of Physical Oceanography*, 45(3), 613–629.
- Montégut, C. B., Madec, G., Fischer, A. S., Lazar, A., & Iudicone, D. (2004). Mixed layer depth over the global ocean: An examination of profile data and a profile-based climatology. *Journal of Geophysical Research*, 109(C12). <https://doi.org/10.1029/2004JC002378>
- Morozov, E. G. (1995). Semidiurnal internal wave global field. *Deep Sea Research Part I: Oceanographic Research Papers*, 42(1), 135–148.
- Morvan, M., L'Hégaret, P., Carton, X., Gula, J., Vic, C., de Marez, C., et al. (2019). The life cycle of submesoscale eddies generated by topographic interactions. *Ocean Science*, 15(6), 1531–1543. <https://doi.org/10.5194/os-15-1531-2019>
- Nagai, T., Tandon, A., Yamazaki, H., Doubell, M. J., & Gallagher, S. (2012). Direct observations of microscale turbulence and thermohaline structure in the Kuroshio Front. *Journal of Geophysical Research*, 117(C8). <https://doi.org/10.1029/2011JC007228>
- Napolitano, D. C., Silveira, I. C. A., Rocha, C. B., Flierl, G. R., Calil, P. H. R., & Martins, R. P. (2019). On the steadiness and instability of the intermediate western boundary current between 24 and 18 S. *Journal of Physical Oceanography*, 49(12), 3127–3143. <https://doi.org/10.1175/JPO-D-19-0011.1>
- Naveira Garabato, A. C., Frajka-Williams, E. E., Spingys, C. P., Legg, S., Polzin, K. L., Forryan, A., et al. (2019). Rapid mixing and exchange of deep-ocean waters in an abyssal boundary current. *Proceedings of the National Academy of Sciences*, 116(27), 13233–13238. <https://doi.org/10.1073/pnas.1904087116>
- Naveira Garabato, A. C., Polzin, K. L., King, B. A., Heywood, K. J., & Visbeck, M. (2004). Widespread intense turbulent mixing in the Southern Ocean. *Science*, 303(5655), 210–213.
- Nikurashin, M., & Ferrari, R. (2010). Radiation and dissipation of internal waves generated by geostrophic motions impinging on small-scale topography: Application to the Southern Ocean. *Journal of Physical Oceanography*, 40(9), 2025–2042. <https://doi.org/10.1175/2010JPO4315.1>
- Omand, M. M., D'Asaro, E. A., Lee, C. M., Perry, M. J., Briggs, N., Cetinić, I., & Mahadevan, A. (2015). Eddy-driven subduction exports particulate organic carbon from the spring bloom. *Science*, 348(6231), 222–225.
- Paiva, A. M., Daher, V. B., Costa, V. S., Camargo, S. S., Mill, G. N., Gabioux, M., & Alvarenga, J. B. (2018). Internal tide generation at the Vitória-Trindade Ridge, South Atlantic Ocean. *Journal of Geophysical Research: Oceans*, 123(8), 5150–5159. <https://doi.org/10.1029/2017JC013725>
- Pérez, J. G. C., & Calil, P. H. R. (2017). Regional turbulence patterns driven by meso- and submesoscale processes in the Caribbean Sea. *Ocean Dynamics*, 67(9), 1217–1230.
- Pollard, R. T., & Regier, L. A. (1992). Vorticity and vertical circulation at an ocean front. *Journal of Physical Oceanography*, 22(6), 609–625.
- Ramachandran, S., Tandon, A., Mackinnon, J., Lucas, A. J., Pinkel, R., Waterhouse, A. F., et al. (2018). Submesoscale processes at shallow salinity fronts in the Bay of Bengal: Observations during the Winter Monsoon. *Journal of Physical Oceanography*, 48(3), 479–509.
- Rocha, C. B., Chereskin, T. K., Gille, S. T., & Menemenlis, D. (2016a). Mesoscale to submesoscale wavenumber spectra in Drake Passage. *Journal of Physical Oceanography*, 46(2), 601–620. <https://doi.org/10.1175/JPO-D-15-0087.1>
- Rocha, C. B., Gille, S. T., Chereskin, T. K., & Menemenlis, D. (2016b). Seasonality of submesoscale dynamics in the kuroshio extension. *Geophysical Research Letters*, 43(21), 11–304. <https://doi.org/10.1002/2016GL071349>
- Rogers, A. D. (2019). Threats to seamount ecosystems and their management. In C. Sheppard (Ed.), *World seas: An environmental evaluation* (pp. 427–451). Amsterdam, Netherlands: Elsevier. <https://doi.org/10.1016/B978-0-12-805052-1.00018-8>
- Ruan, X., Thompson, A. F., Flexas, M. M., & Sprintall, J. (2017). Contribution of topographically generated submesoscale turbulence to Southern Ocean overturning. *Nature Geoscience*, 10(11), 840–845.
- Rudnick, D. L. (1996). Intensive surveys of the Azores front: 2. Inferring the geostrophic and vertical velocity fields. *Journal of Geophysical Research*, 101(C7), 16291–16303.
- Rudnick, D. L. (2001). On the skewness of vorticity in the upper ocean. *Geophysical Research Letters*, 28(10), 2045–2048.
- Sasaki, H., Klein, P., Qiu, B., & Sasai, Y. (2014). Impact of oceanic-scale interactions on the seasonal modulation of ocean dynamics by the atmosphere. *Nature Communications*, 5(1), 1–8.
- Sasaki, H., Klein, P., Sasai, Y., & Qiu, B. (2017). Regionality and seasonality of submesoscale and mesoscale turbulence in the North Pacific Ocean. *Ocean Dynamics*, 67(9), 1195–1216.
- Schmid, C., & Majumder, S. (2018). Transport variability of the Brazil current from observations and a data assimilation model. *Ocean Science*, 14(3), 417–436. <https://doi.org/10.5194/os-14-417-2018>. Retrieved from <https://os.copernicus.org/articles/14/417/2018/>
- Schmid, C., Schäfer, H., Zenk, W., & Podestà, G. (1995). The Vitória eddy and its relation to the Brazil Current. *Journal of Physical Oceanography*, 25(11), 2532–2546.
- Shchepetkin, A. F., & McWilliams, J. C. (2005). The regional oceanic modeling system (ROMS): A split-explicit, free-surface, topography-following-coordinate oceanic model. *Ocean Modelling*, 9(4), 347–404.
- Shcherbina, A. Y., D'Asaro, E. A., Lee, C. M., Klymak, J. M., Molemaker, M. J., & McWilliams, J. C. (2013). Statistics of vertical vorticity, divergence, and strain in a developed submesoscale turbulence field. *Geophysical Research Letters*, 40(17), 4706–4711. <https://doi.org/10.1002/grl.50919>
- Silveira, I. C. A., Calado, L., Castro, B. M., Cirano, M., Lima, J. A. M., & Mascarenhas, A. S. (2004). On the baroclinic structure of the Brazil current-intermediate western boundary current system at 22–23 S. *Geophysical Research Letters*, 31(14), L14308. <https://doi.org/10.1029/2004GL020036>
- Silveira, I. C. A., Lima, J. A. M., Schmidt, A. C. K., Ceccopieri, W., Sartori, A., Francisco, C. P. F., & Fontes, R. F. C. (2008). Is the meander growth in the Brazil Current system off Southeast Brazil due to baroclinic instability? *Dynamics of Atmospheres and Oceans*, 45(3), 187–207. <https://doi.org/10.1016/j.dynatmoe.2008.01.002>

- Soutelino, R. G., Gangopadhyay, A., & Silveira, I. C. (2013). The roles of vertical shear and topography on the eddy formation near the site of origin of the Brazil Current. *Continental Shelf Research*, 70, 46–60. <https://doi.org/10.1016/j.csr.2013.10.001>
- Soutelino, R. G., Silveira, I. C. A., Gangopadhyay, A. A. M. J., & Miranda, J. A. (2011). Is the Brazil Current eddy-dominated to the north of 20 S?. *Geophysical Research Letters*, 38(3). <https://doi.org/10.1029/2010GL046276>
- Stamper, M. A., & Taylor, J. R. (2017). The transition from symmetric to baroclinic instability in the Eady model. *Ocean Dynamics*, 67(1), 65–80.
- Stern, M. E. (1985). Lateral wave breaking and “shingle” formation in large-scale shear flow. *Journal of Physical Oceanography*, 15(10), 1274–1283.
- Stone, P. H. (1966). On non-geostrophic baroclinic stability. *Journal of the Atmospheric Sciences*, 23(4), 390–400.
- Taylor, J. R., & Ferrari, R. (2010). Buoyancy and wind-driven convection at mixed layer density fronts. *Journal of Physical Oceanography*, 40(6), 1222–1242. <https://doi.org/10.1175/2010JPO4365.1>
- Thomas, L. N., Tandon, A., & Mahadevan, A. (2008). Submesoscale processes and dynamics. In M. W. Hecht, H. Hasumi (Eds.), *Geophysical Monograph Series, Ocean modeling in an eddying regime* (Vol. 177, pp. 17–38). Hoboken, NJ: Wiley. <https://doi.org/10.1029/177GM04>
- Thomas, L. N., Taylor, J. R., D’Asaro, E. A., Lee, C. M., Klymak, J. M., & Shcherbina, A. (2016). Symmetric instability, inertial oscillations, and turbulence at the Gulf Stream front. *Journal of Physical Oceanography*, 46(1), 197–217.
- Thomas, L. N., Taylor, J. R., Ferrari, R., & Joyce, T. M. (2013). Symmetric instability in the Gulf stream. *Deep Sea Research Part II: Topical Studies in Oceanography*, 91, 96–110.
- Thompson, A. F., Lazar, A., Buckingham, C., Naveira Garabato, A. C., Damerell, G. M., & Heywood, K. J. (2016). Open-ocean submesoscale motions: A full seasonal cycle of mixed layer instabilities from gliders. *Journal of Physical Oceanography*, 46(4), 1285–1307.
- Viglione, G. A., Thompson, A. F., Flexas, M. M., Sprintall, J., & Swart, S. (2018). Abrupt transitions in submesoscale structure in Southern Drake Passage: Glider observations and model results. *Journal of Physical Oceanography*, 48(9), 2011–2027.
- Voosen, P. (2018). Fleet of sailboat drones could monitor climate change’s effect on oceans. *Science Magazine*. Retrieved from <https://www.sciencemag.org/news/2018/03/fleet-sailboat-drones-could-monitor-climate-change-s-effect-oceans>; <https://doi.org/10.1126/science.aat5323>
- Wenegrat, J. O., Thomas, L. N., Gula, J., & McWilliams, J. C. (2018). Effects of the submesoscale on the potential vorticity budget of ocean mode waters. *Journal of Physical Oceanography*, 48(9), 2141–2165.
- Whalen, C. B., de Lavergne, C., Garabato, A. C. N., Klymak, J. M., MacKinnon, J. A., & Sheen, K. L. (2020). Internal wave-driven mixing: Governing processes and consequences for climate. *Nature Reviews Earth & Environment*, 1, 606–621. <https://doi.org/10.1038/s43017-020-0097-z>
- Whitt, D. B., Thomas, L. N., Klymak, J. M., Lee, C. M., & D’Asaro, E. A. (2018). Interaction of superinertial waves with submesoscale cyclonic filaments in the north wall of the gulf stream. *Journal of Physical Oceanography*, 48(1), 81–99.
- Zhao, Z., Alford, M. H., Girton, J. B., Rainville, L., & Simmons, H. L. (2016). Global observations of open-ocean mode-1 m2 internal tides. *Journal of Physical Oceanography*, 46(6), 1657–1684.